AGU PUBLICATIONS

Geophysical Research Letters

Supporting Information for

Internal ocean-atmosphere variability drives megadroughts in Western North America

S. Coats[1], J. E. Smerdon[2], B. I. Cook[3,2], R. Seager[2], E. R. Cook[2], K. J. Anchukaitis[4]

[1]Cooperative Institute for Research in Environmental Sciences, University of Colorado, Boulder, Colorado
[2]Lamont-Doherty Earth Observatory of Columbia University, Palisades, New York
[3]NASA Goddard Institute for Space Studies, New York, New York
[4]Department of Geography and Development and Laboratory of Tree Ring Research, University of Arizona, Tucson, Arizona

Contents of this file

Text S1 to S2
Figures S1 to S9
Table S1 to S3

Introduction

The supplementary information contains the full description of the data and the methodology and methodological validation, as well as a brief discussion of the methodology in the context of the results presented in the main manuscript.

Text S1.

A. Megadroughts and Available ENSO Reconstructions

The right hand panels of Figure S1 show five published ENSO and eastern tropical Pacific SST reconstructions, which are not fully independent but are calculated using different reconstruction methods and proxy networks. There is only weak agreement between the overall time history of the five reconstructions and large differences in the magnitudes and variability structures (only three of the ten possible correlations between reconstructions are significant at the 99% level). To focus specifically on the dynamics that coincide with the five identified megadroughts, the left hand panel of Figure S1 indicates the percentage of megadrought years that have positive or negative values in each of the reconstructions. In aggregate, the reconstructions suggest that ENSO tends to be negative during megadroughts. This is perhaps unsurprising given that the reconstructions, with the exception of *Tierney et al.* [*2015*], use the North American tree-ring chronologies in which megadroughts were identified. Nevertheless, of the 16 times that the five identified megadroughts overlap with the reconstructions only five are individually significant at the 95% level using a distribution and autocorrelation preserving bootstrapping significance test (Text S2 Section G). The ambiguity of the relationship between reconstructed ENSO conditions and megadroughts provides a strong motivation for the research that we present herein.

B. Independent Steps of the Climate Analogues Framework

The feasibility of using the drought atlases in the climate analogues framework requires multiple levels of independence, each of which are described herein. First, many large-scale field reconstructions would not be appropriate to use in the climate analogues framework because they calibrate on large-scale patterns of variability. These joint space/time reconstruction methods, such as canonical correlation analysis [*Smerdon et al. ,2010*] or regularized expectation maximization [e.g. *Mann et al., 2009*], differ from the point-by-point regression specifically used to produce the drought atlases. Point-by-point regression is a sequential principal components regression between tree-ring chronologies and PDSI at each grid point. Importantly, the method is based on the premise of "local control" [*Cook et al., 2007*], only utilizing chronologies within a fixed search radius centered on each grid point, and thus all large-scale patterns within the drought atlases are emergent. This characteristic is critical for our purposes because the climate analogues framework relies on pattern comparisons. The one caveat is that the fixed search radius used to define the zone of "local control" in point-by-point regression produces spatial smoothing, but the scale of the smoothing is small compared to the spatial scales of the drought atlas domains. Secondly, the instrumental SST and surface pressure data used to define the impact maps are independent from the drought atlases, thus any relationships between the two are likewise emergent. Finally, the drought atlases are each individually independent, with no shared chronologies or calibration data. This characteristic is also critical for our purposes because the climate analogues framework is used to determine the dynamics that coincide with megadroughts (Figure 1B) that are identified within the NADA. The independence of the drought atlases allows us to recompute the climate analogues framework over the individual drought atlas domains (and combinations) to provide confidence that any megadrought dynamics are robust and not solely dependent on teleconnections to the NADA (Figure 1C).

C. Megadrought Composites

The five identified megadroughts are consistently and significantly associated with tropical Pacific cold states (Figure 1). Despite the consistent relationship between megadroughts and the tropical Pacific Ocean, there are differences in the pattern of reconstructed hydroclimate when the drought atlases are composited for each megadrought (Figure 2, left panels). This is unsurprising given that modes of atmosphere, ocean and coupled variability outside of the tropical Pacific Ocean (including the PDO, AMO and NAO analyzed herein) will also impact hydroclimate during megadroughts, even if they are not the primary dynamical driver of these features. The right hand panels of Figure 2 show composites of the highest CPCS impact maps for each year of the five identified megadroughts (the highest CPCS impact maps determine the state of the four modes of variability in Figure 1). There is considerable agreement between the composites in the left and right hand panels of Figure 2, suggesting that the megadrought dynamics implied by the climate analogues framework, namely a negative ENSO state and the various states of the other three modes of variability (there is little consistency of these three modes during megadroughts), can produce the composite hydroclimate patterns of megadroughts. Any disagreement in the composite patterns in Figure 2, however, can be explained by modes of atmosphere-ocean or stochastic atmospheric variability that were not analyzed herein or out-of-sample combinations of the four analyzed modes of variability (given the short instrumental record, see sufficient sampling restriction in Section 3 of the main manuscript). Importantly, the results in Figure 2 suggest that neither of these sources of error is large in magnitude.

D. AMO During the MCA

As is noted in the main manuscript, the predominately positive AMO during the MCA (Figure 1A) can potentially help explain the clustering and severity of megadroughts during this period. Nevertheless, it is difficult for the climate analogues framework to reproduce the state of the AMO because of poor sampling of such low-frequency modes over the 135-year training interval (Figures S3, S4, S5, S6 and Text S2 Sections A-C). There is, however, other evidence (some independent) for a positive AMO during the MCA. Firstly, the shift to a positive AMO in Figure 1A (~1100 C.E.) is coincident with a period of protracted drying in the Central Plains and Mississippi Valley regions of NA [*Cook et al., 2010a*], where hydroclimate variability is often coupled to Atlantic SSTs [*Kushnir et al., 2010; McCabe et al., 2004*]. Secondly, Feng et al. [*2008*] analyze multiple in situ proxies of North Atlantic SSTs and find warm conditions in the Atlantic during the MCA that are characteristic of a positive AMO. When taken together with the results presented herein, namely that the temporal clustering and character of tropical Pacific cold states during the MCA is not unique and that the Northern Hemisphere tree-ring record also suggests a positive AMO during the MCA, this provides compelling evidence for a role for the AMO in driving the severity and clustering of MCA megadroughts. Nevertheless, recent research has also suggested that the AMO is a response of the ocean to forcing by stochastic atmospheric variability [*Clement et al., 2015*], which might preclude the AMO having centennial scale persistence or being able to drive a precipitation response over land. Further evaluating the state of the AMO during the MCA and the relationships between the atmosphere and North Atlantic Ocean are important areas of future research.

E. PDO During the MCA

Figure 1A suggests that the PDO was positive during much of the MCA. In observations, however, a positive PDO actually produces wetting over the American West [*McCabe et al., 2004*]. A persistently positive PDO during the MCA is likewise inconsistent with the results of Macdonald and Case [*2005*], in which western NA tree-ring chronologies were used to reconstruct a negative PDO for the first half of the last millennium. Evidence here from the full Northern Hemisphere tree-ring record is therefore inconsistent with the MCA PDO signal within the western NA tree-ring chronologies employed by Macdonald and Case [*2005*]. Nevertheless, the pseudoproxy experiments used for methodological validation provide less confidence in this result and the PDO output of the climate analogues framework appears sensitive to the choice of observational dataset (Text S2 Section D). A recent reconstruction of bi-hemispheric interdecadal Pacific variability, however, also suggests that the PDO was positive during the MCA [*Vance et al., 2015*].

F. NAO During the MCA

There is little consistency to the NAO during the MCA, or more generally, during megadroughts (Figure 1). This is interesting given prior evidence, based partially on tree-rings, that the NAO was in a positive state for the entirety of the MCA [*Truoet et al., 2009*]. Nevertheless, recent research into the state of the NAO during the MCA using multiple proxies, model simulations and pseudoproxy experiments appears much more consistent with the results presented herein [*Ortega et al., 2015*].

Text S2.

A. Pseudoproxy Experiments

Four 500-year control simulations are used in a pseudoproxy context to test the climate analogues framework (CCSM4, GISS-E2-R, IPSL-CM5A-LR, MPI-ESM-P in Table S1). These simulations were distributed through the Climate Model Intercomparison Project phase 5 (CMIP5—*Taylor et al.* [*2012*]). The use of multiple models is important given research that suggests skill in pseudoproxy experiments is model dependent [*Smerdon et al., 2016*] and the four models were chosen to sample a range in the characteristics of simulated decadal-to-multidecadal atmosphere-ocean dynamics [*Coats et al., 2015b*].

The climate analogues framework is computed using the same grid points as the NADA, MADA and OWDA, but with white noise added to the PDSI fields from each model to produce a signal-to-noise ratio of 0.5, which approximates the level of noise within the NADA [*Cook et al., 2007*]. To best mimic the characteristics of the actual climate analogues framework, the impact maps are calculated eight times, each corresponding to a different 135-year (length of the instrumental interval) training interval. Because the CGCM simulations are only 500 years in length, there are fewer than 4 fully independent 135-year intervals. There must, therefore, be some overlap between each of the eight 135-year training intervals. Nevertheless no two training intervals share more than 85 years and there is an average overlap between training intervals of just 29 years.

B. Pseudoproxy Timeseries

Figures S3 and S4 provide a visual representation of the dynamical timeseries produced by the climate analogues framework within the pseudoproxy experiments. In both figures the model ground truth is plotted for comparison. Skill is measured herein as the fraction of years outside of the training interval in which the dynamical timeseries from the climate analogues framework is the correct sign relative to the model ground truth. This metric is motivated by the analysis in Panels B and C of Figure 1, which only assesses whether the ENSO, AMO, PDO and NAO are positive or negative during each megadrought. Nevertheless, a more complicated skill metric such as normalized root-mean squared error produces similar results and interpretation (Figure S6 and Text S2 Section C). For each model and mode, Figure S3 plots the dynamical timeseries corresponding to the best (highest skill) and worst instrumental-length (135-year) training interval. For comparison, Figure S4 plots the dynamical timeseries corresponding to impact maps calculated over the full temporal extent of the model simulations.

The visual representations in Figure S3 indicate that for all models and modes the best timeseries (highest skill—red lines) reproduce much of the time history of the model ground truth. Even for the worst ENSO and NAO timeseries (lowest skill—blue lines), the dominant features of the time history of the ground truth is still reproduced. This provides confidence that the climate analogues framework will provide useful information for defining the state of the ENSO and NAO during megadroughts. The worst timeseries of the PDO and AMO, however, struggle to reproduce the time history of these modes. Importantly, the climate analogues framework is able to reproduce the dominant timescales of variability for all four modes, with the AMO and PDO having more persistence (and thus larger magnitudes in Figure S3) relative to the ENSO and NAO.

The dynamical timeseries associated with impact maps calculated over the full temporal extent of the model simulations are nearly perfect representations of the model ground truth (Figure S4). Any inability to reproduce these modes of variability, therefore, appears to be related to the short 135-year training intervals providing too few degrees of freedom to properly constrain their impact on hydroclimate over the Northern Hemisphere. This is particularly true of the PDO and AMO because of the longer timescales of variability inherent to these modes. Importantly, this will be a fundamental limitation of any method that trains on the instrumental record, including any indirect (i.e. not based on local proxies that directly sample the variable of interest, in this case SSTs) reconstructions of these modes and particularly those using land-based proxies. Nevertheless, model representation of the PDO and AMO, and their hydroclimate impacts, is poor [*Coats et al., 2015b*]. In particular, the teleconnections between these modes and Northern Hemisphere land areas appear weaker than those observed over the instrumental record. This presents a critical caveat for the pseudoproxy experiments performed herein and given this, the pseudoproxy-derived skill for these modes may be a pessimistic representation of potential skill.

C. Skill Scores

To explicitly define the skill of the climate analogues framework, Figure S5 plots the fraction of years during the non-training interval in which the dynamical timeseries is the correct sign relative to the real ENSO, PDO, AMO and NAO from the model output. The boxplots demonstrate the range in skill for the eight instrumental-length training intervals and the asterisks indicate the skill value if the impact maps are calculated over the full temporal extent of the model simulations. We calculate a significant skill threshold by randomly generating the positive, negative or neutral state of each mode in each year 1,000 times and assessing the 95th percentile of skill for these randomly generated timeseries (skill below the thresholds are plotted as the grey shaded regions in Figure S5). Additionally, to test the benefit provided by using the collection of drought atlases, the pseudoproxy skill is calculated for a climate analogues framework using just the individual regions covered by the NADA, MADA and OWDA (and combinations—boxplot colors in Figure S5).

As was suggested by the visual representations in Figures S3 and S4, given enough degrees of freedom, the climate analogues framework will be highly skillful (asterisks in Figure S5). For instrumental-length training intervals, however, the climate analogues framework is only significantly skillful for the ENSO and NAO and this behavior is not highly model dependent. Finally, using the NADA, MADA and OWDA regions together provides additional skill relative to a climate analogues framework calculated using only individual regions. Figure S6 shows the same information as Figure S5 but using normalized root mean-squared error (NRMSE) as the skill metric. As noted previously, the use of a more complicated skill metric like NRMSE provides similar results and interpretation to Figure S5. This further suggests that the skill metric in Figure S5, which was chosen to be easily interpretable with respect to the results in Figure 1, is a robust metric of the skill of the climate analogues framework.

D. Sensitivity to Choice of Observational Dataset

To test the sensitivity of the methodology and results to the choice of observational dataset, the climate analogues framework was recalculated using Kaplan ESSTv2 [Kaplan et al., 1998] and COBE2 [Hirahara et al., 2014] SST datasets. While there are differences in the 154 impact maps calculated based on the three different SST datasets (Figure S7), there is good agreement in the output of the climate analogues frameworks based on these impact maps (both in terms of correlation and the fraction of years in which the dynamical timeseries from the climate analogues framework have the same sign—inset of Figure S7). Most importantly, there is little difference in the megadrought associations derived from the three different climate analogues frameworks with 96%, 91% and 91% of megadrought years having negative ENSO values for the NOAA ERSSTv3b, Kaplan EESTv2, and COBE2 datasets, respectively. The only difference in megadrought associations is that there is a statistically significant negative association between megadroughts and a negative PDO for the Kaplan ESSTv2 dataset.

E. Sensitivity to Tree-ring Site Distribution and Density

The distribution and density of tree-ring sites changes through time in the NADA, MADA and OWDA. For instance, while the NADA contains nearly 2000 chronologies, there are only 100 in 1000 C.E. (the beginning of the analysis period—Figure S8). To test that the distribution and density of tree-ring sites at the beginning of the analysis period is sufficient to conduct the spatial analyses underlying the climate analogues framework we recalculate the framework using only grid points within a fixed distance (search radius) of available tree-ring sites. Table S2 shows the skill of these climate analogues frameworks (three different search radii and two different starting dates) over the observational training interval (1871-2005 C.E.—calculated as the fraction of years in which the dynamical timeseries from the climate analogues framework have the same sign as the observations). Even with the most limited grid (1000 C.E. starting date and 150 km search radius) the climate analogues framework can largely reproduce the observed history of the four modes of variability. This analysis provides confidence that climate analogues framework can derive useful information on these modes of variability from the distribution and density of tree-ring sites in 1000 C.E.

F. MCA Mean Shift

In order to provide confidence in the interpretation of the atmosphere-ocean conditions during the MCA (Figures 1 and 3) relative to previous hypotheses [e.g. *Herweijer et al., 2007; Seager et al., 2007; Graham et al., 2007*], we must confirm that the climate analogues framework can capture a centuries long shift in the mean of central and eastern equatorial Pacific SSTs (tropical Pacific mean shift). To do so, we identified a 300-year period (the length of the MCA) with a tropical Pacific mean shift in the MIROC last millennium simulation from the CMIP5 (a forced transient simulation covering 850-1849 C.E.—Table S1). We then used the perfect sampling of the model to determine if the climate analogues framework can reproduce this tropical Pacific mean shift. Importantly, the MIROC last millenium simulation has a drift with a positive trend of 0.11 °C/century in global temperatures between 850-1849 C.E. Superimposed on the globally cooler conditions in years 850-1149 C.E., however, is an increase in the zonal gradient of SSTs across the tropical Pacific Ocean (Panel A of Figure S9). This tropical Pacific mean shift impacts hydroclimate over the Northern Hemisphere—while the composite of PDSI between 850-1149 C.E. is wet across the Northern Hemisphere, with globally cooler temperatures decreasing atmospheric demand for moisture, there are zonal and meridional inhomogeneities in the pattern of PDSI. These inhomogeneties (and thus the overall pattern) are consistent (CPCS of 0.65) with the expected impact of a negative ENSO state as defined between 1871-2005 C.E. in the MIROC historical simulation also from the CMIP5 (Panel B of Figure S9). To test if the climate analogues framework can reproduce this 300-year tropical Pacific mean shift we define impact maps over the 1871-2005 C.E. period in the MIROC historical simulation. We then calculate the climate analogues framework for the MIROC last millennium simulation (850-1849 C.E.) following the same set up as the pseudoproxy experiments in Text S2 Section A. Panel C of Figure S9 indicates that the climate analogues framework is largely successful at reproducing the tropical Pacific mean shift between 850-1149 C.E. Importantly, the shift in the mean of the Niño3.4 index in the MIROC simulation during this period is smaller than the mean of the Niño3 index implied by *Mann et al.* [*2009*] during the MCA (1000-1299 C.E.). This comparison clearly suggests that the success of the climate analogues framework in reproducing the tropical Pacific mean shift in the MIROC simulation does not arise because it is unreasonably large in magnitude. Together these results provide confidence that the climate analogues framework would reproduce a centuries long shift in the mean of central and eastern equatorial Pacific SSTs if it did exist. For reference, 57% of years have a negative ENSO state in the actual climate analogues framework (Figure 1A) during the MCA (1000-1299 C.E.). This is clearly inconsistent with the tropical Pacific mean shift between 850-1149 C.E. in the MIROC simulation where 70% of years have a negative ENSO state. As noted above, the tropical Pacific mean shift between 850-1149 C.E. in the MIROC simulation is also smaller in magnitude and less consistent than the tropical Pacific mean shift implied by *Mann et al.* [*2009*—Figure S9].

G. Significance Testing

To test the statistical significance of the association between megadroughts and the four modes of variability we use a bootstrapping method [*Schrieber and Schmitz, 2000*] to produce 5000 surrogate timeseries that exactly preserve the distribution of the timeseries in Figure 1A, while largely preserving the spectral characteristics (there will be a slight whitening of the surrogate spectrum). Significance at the 95% level is achieved if the positive or negative state of the timeseries in Figure 1A is coincident with megadrought years at a percentage greater than 95% of the surrogate timeseries; this assessment is performed for each individual megadrought (to produce the range in the 95% significance levels in Panel B of Figure 1) and for all five megadroughts together (Panel B and Panel C of Figure 1). This method of assessing statistical significance is equivalent to that used in *Coats et al.* [*2015a*].

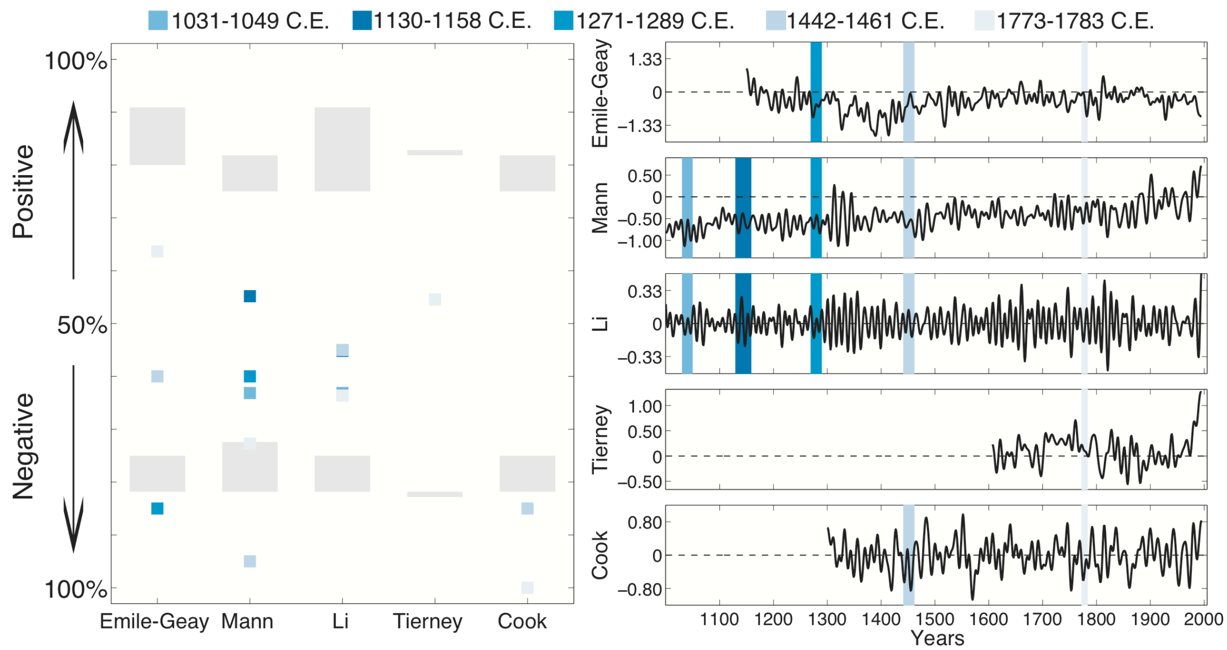

Figure S1. (right) Reconstructions of ENSO using different methods and proxy networks [*Mann et al., 2009; Emile-Geay et al., 2013; Tierney et al., 2015; Li et al., 2013; Cook et al., 2009*]. In each case the data has been ten-year lowpass filtered. For *Emile-Geay et al.* [*2013*], *Li et al.* [*2013*], *Cook et al.* [*2009*] the reconstructed index is for the Niño3.4 region, while for *Mann et al.* [*2009*] it is the Niño3 region and for [*Tierney et al., 2015*] it is the eastern Pacific (10°N-10°S, 175°E-85°W). The timing of the five identified megadroughts is denoted by the colored regions. (left) Associations between the identified megadroughts and ENSO for the period 1000-2005 C.E. using linearly detrended timeseries as some reconstructions are standardized against a warm instrumental interval [e.g., [*Mann et al., 2009*] and by consequence are always anomalously negative outside of that interval]. Similar conclusions are found if a mean offset is used (not shown). The colored squares are for the five identified megadroughts [less than five of these features, however, overlap with the reconstructed record in *Emile-Geay et al.*, [*2013*], *Tierney et al.* [*2015*], and *Cook et al.* [*2009*]]. The shaded regions are the range in 95% significance level for the five identified megadroughts using a distribution and autocorrelation preserving bootstrapping method to test statistical significance (Text S2 part G).

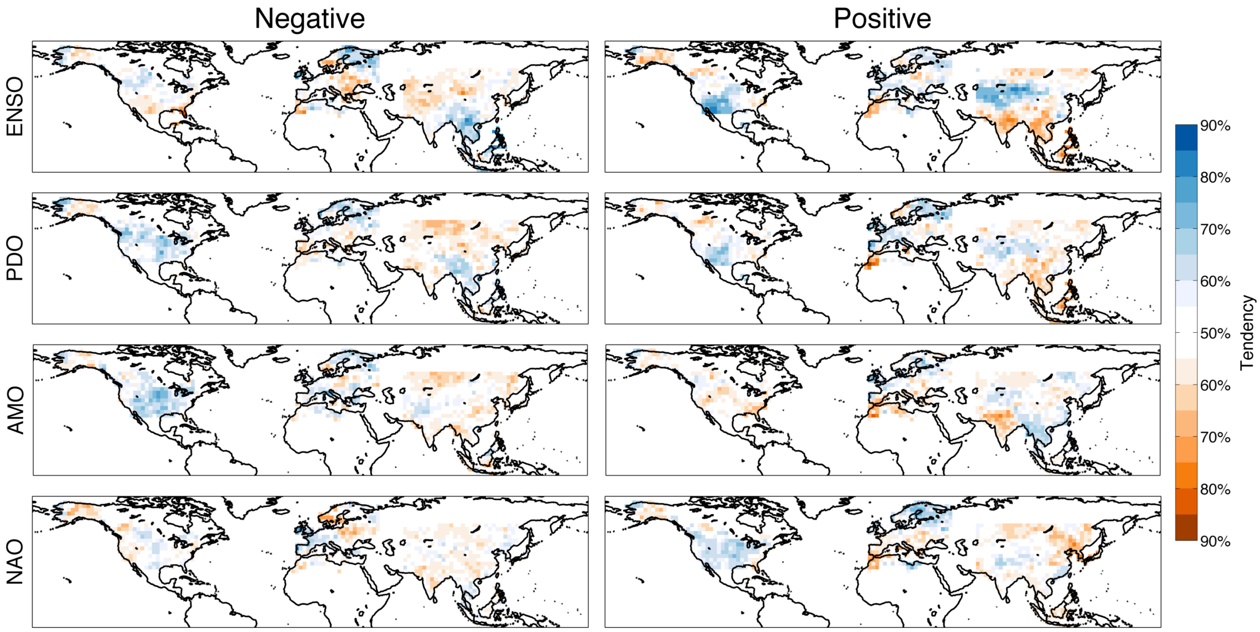

Figure S2. Impact maps corresponding to the positive and negative state (one mode combinations) of each mode of variability. (blue is a wetting tendency, brown is a drying tendency). Tendency is defined as the percentage of years in the composite that were wet or dry at each grid point. As an example, a tendency of 90% dry for positive ENSO would indicate that 90% of years in the top third of ENSO values were dry at that grid point.

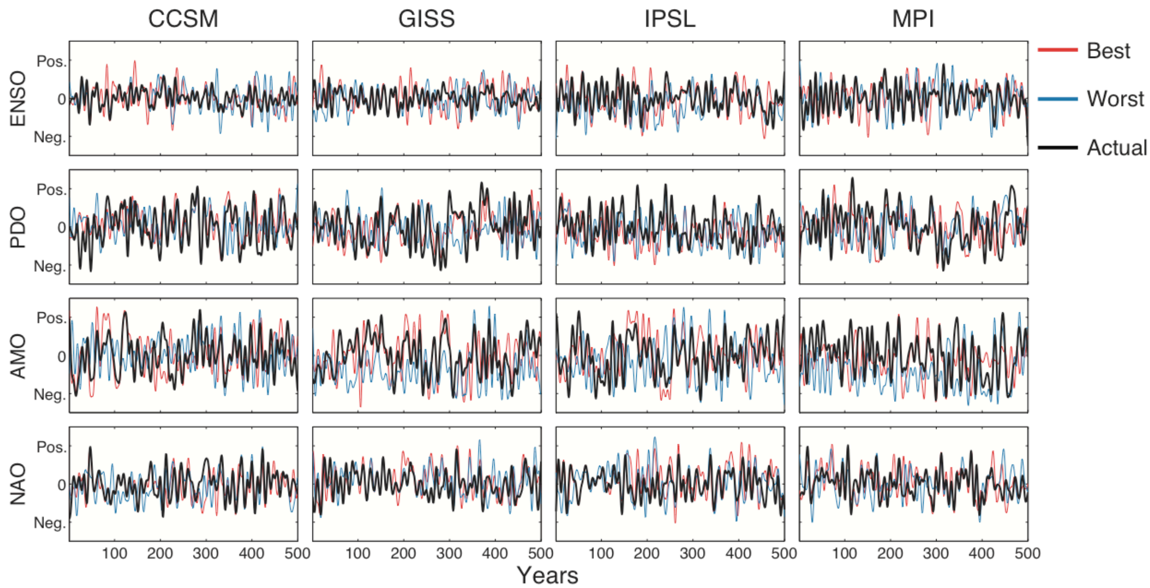

Figure S3. Example dynamical timeseries for each model and mode. In each case the actual time history of the mode is plotted in black with the time history corresponding to the the training interval that produced the worst (blue) and best (red) dynamical timeseries is also plotted. In each case the timeseries are are ten-year lowpass filtered.

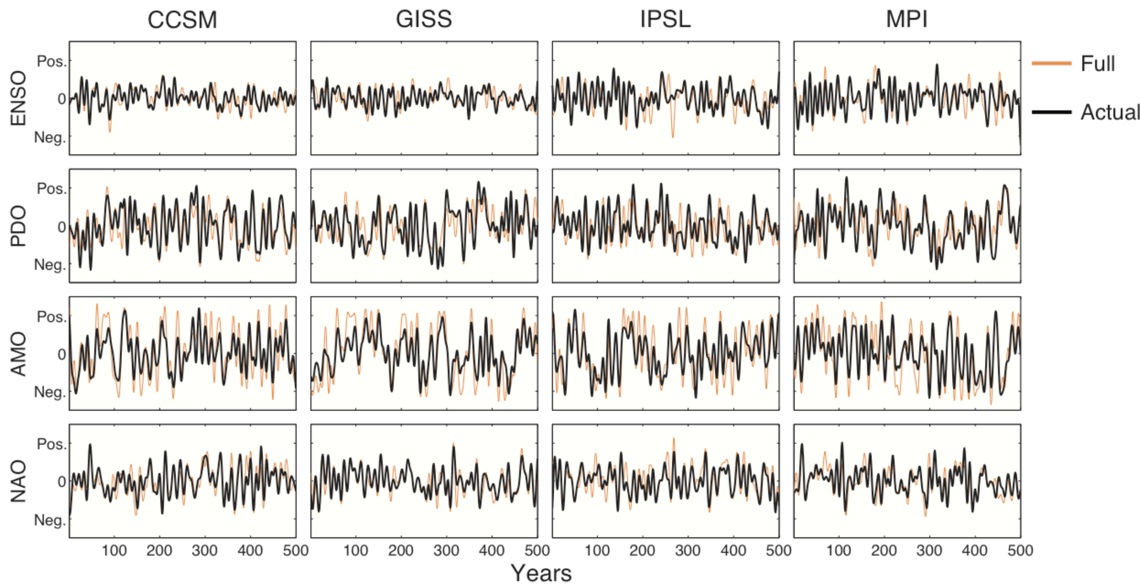

Figure S4. Example dynamical timeseries for each model and mode. In each case the actual time history of the mode is plotted in black with the dynamical timeseries corresponding to the impact maps calculated over the full temporal extent of the model simulations is plotted in orange. In each case the timeseries are are ten-year lowpass filtered.

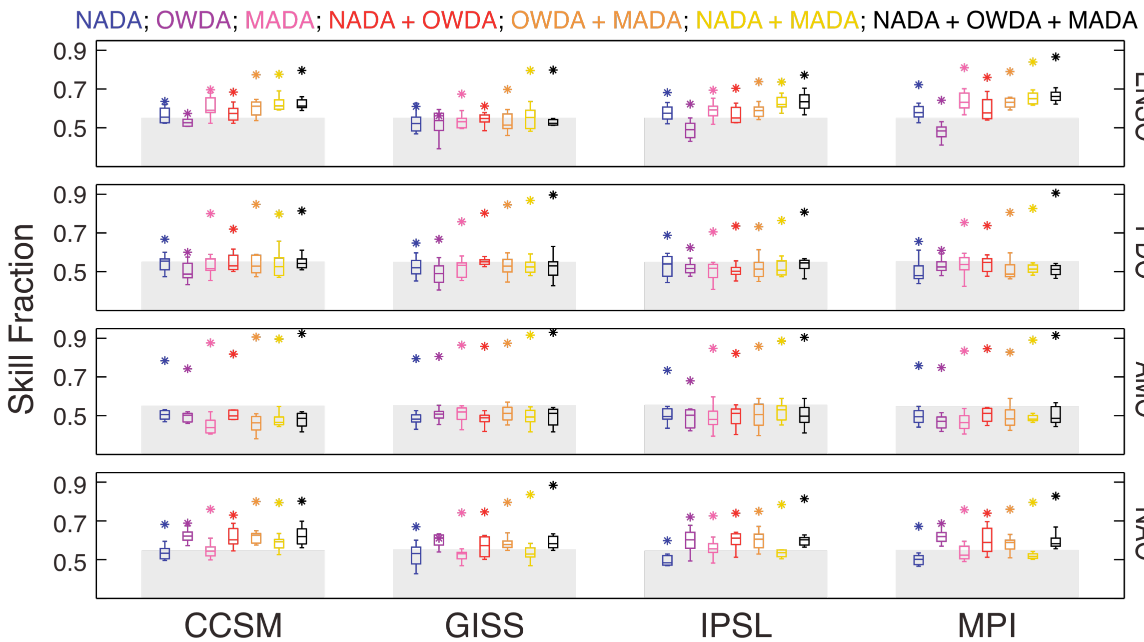

Figure S5. Skill calculated as the fraction of years in which the dynamical timeseries calculated using the climate analogues framework is the correct sign relative to the model ground truth. The asterisk is the skill when using the full temporal extent of the model simulation to compute the impact maps. The boxplots are the range in skill for impact maps calculated using 135-year (length of the instrumental interval) training intervals. For the latter, the skill is calculated only during the non-training interval. Each color corresponds to a climate analogues framework computed using a subset of the full Northern Hemisphere spatial range. Skill below the 95th percentile for randomly generated dynamical timeseries is denoted by the gray shaded region. All pseudoproxies have been calculated using a 0.5 signal-to-noise ratio.

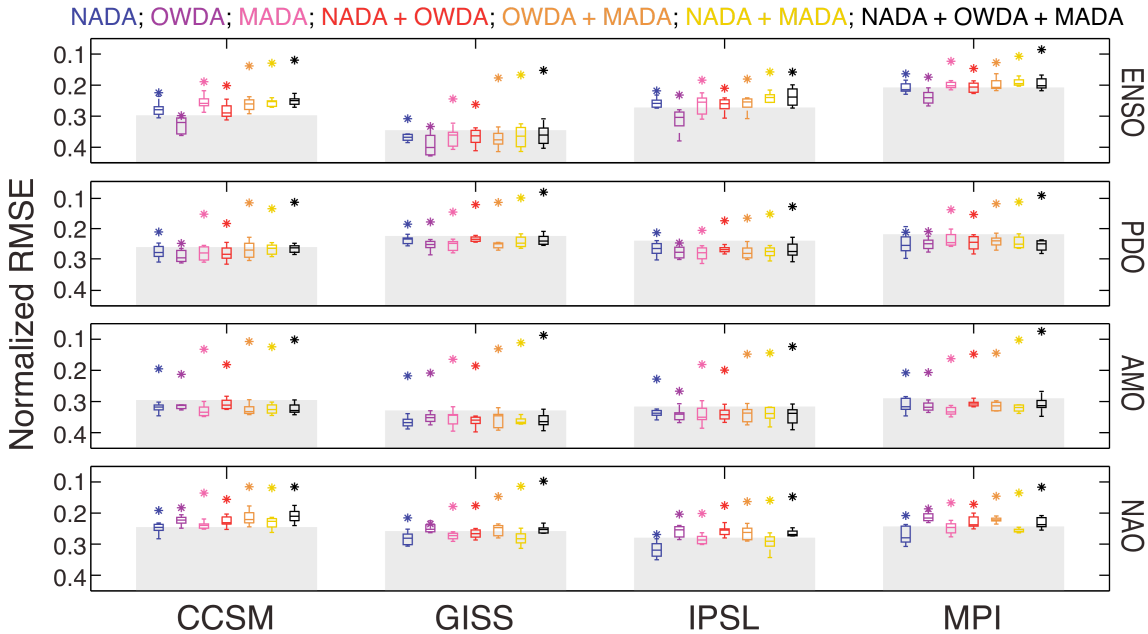

Figure S6. Normalized root-mean squared error (NRMSE) between the dynamical timeseries calculated using the climate analogues framework and the model ground truth. The asterisk is the NRMSE when using the full temporal extent of the model simulation to compute the impact maps. The boxplots are the range in NRMSE for impact maps calculated using 135-year (length of the instrumental interval) training intervals. For the latter, the NRMSE is calculated only during the non-training interval. Each color corresponds to a climate analogues framework computed using a subset of the full Northern Hemisphere spatial range. NRMSE below the 95th percentile for randomly generated dynamical timeseries is denoted by the gray shaded region. All pseudoproxies have been calculated using a 0.5 signal-to-noise ratio.

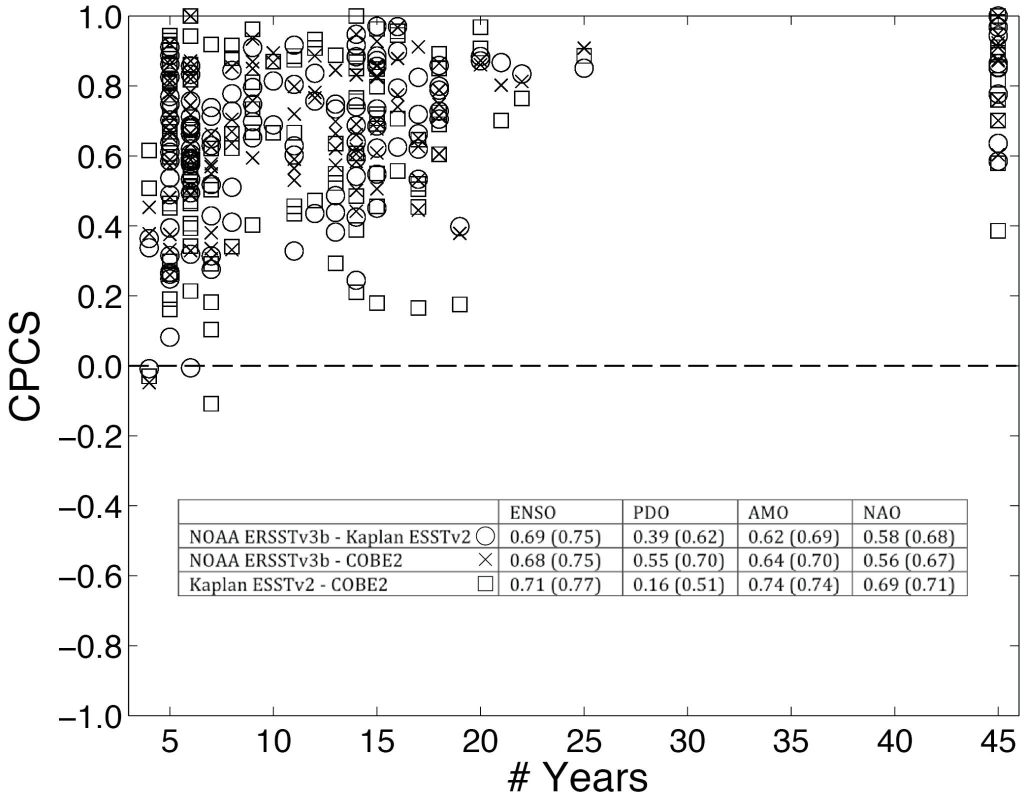

	ENSO	PDO	AMO	NAO
NOAA ERSSTv3b - Kaplan ESSTv2 ○	0.69 (0.75)	0.39 (0.62)	0.62 (0.69)	0.58 (0.68)
NOAA ERSSTv3b - COBE2 ×	0.68 (0.75)	0.55 (0.70)	0.64 (0.70)	0.56 (0.67)
Kaplan ESSTv2 - COBE2 □	0.71 (0.77)	0.16 (0.51)	0.74 (0.74)	0.69 (0.71)

Figure S7. CPCS [*Santer et al., 1995*] between the 154 impact maps based on modes of variability calculated from NOAA ERSTTv3b (used in all analyses—*Smith et al.* [*2003*]), Kaplan ESSTv2 [*Kaplan et al., 1998*] and COBE2 [*Hirahara et al., 2014*]. These are plotted for each combination of datasets (symbols) as a function of the number of years (# Years) during the instrumental training interval that were used to calculate the impact maps. Impact maps corresponding to the modes of variability in isolation are calculated over 45 years, thus this is the largest value on the horizontal axis. There is nothing plotted for number of years between 26-44 because there are no combinations of the states of the four modes of variability that occur over those numbers of years. The inset shows the correlation and fraction of years (parentheses) in which the dynamical timeseries from the three climate analogues frameworks have the same sign for each of the four modes of variability over the full analysis period (1000-2005 C.E.).

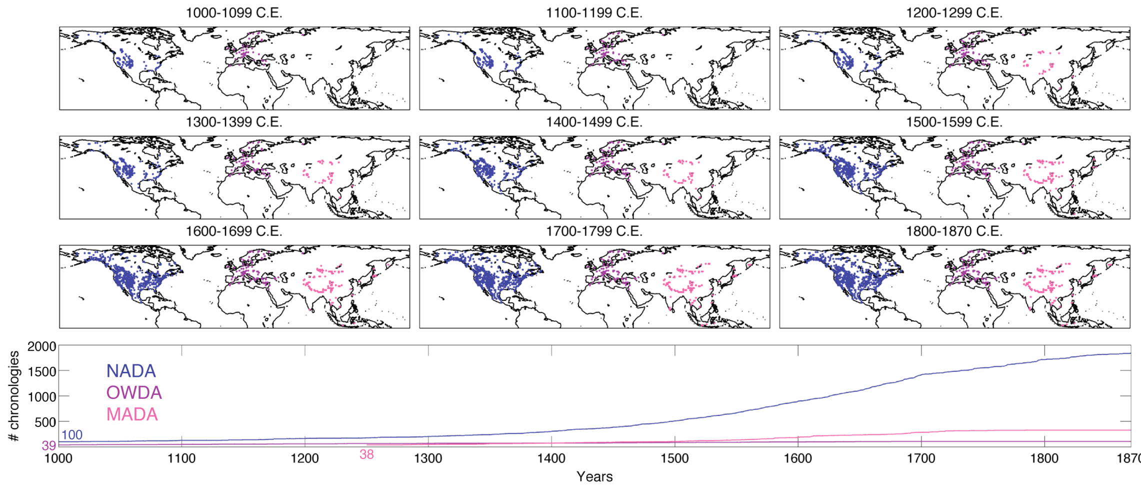

Figure S8. Maps show the distribution of tree-ring sites for each century during the period before the instrumental training interval (1000-1870 C.E.). The bottom panel shows the number of chronologies for the NADA, OWDA and MADA as a function of time, with the minimum number of chronologies during the analysis period listed as the colored number at the starting year of each drought atlas.

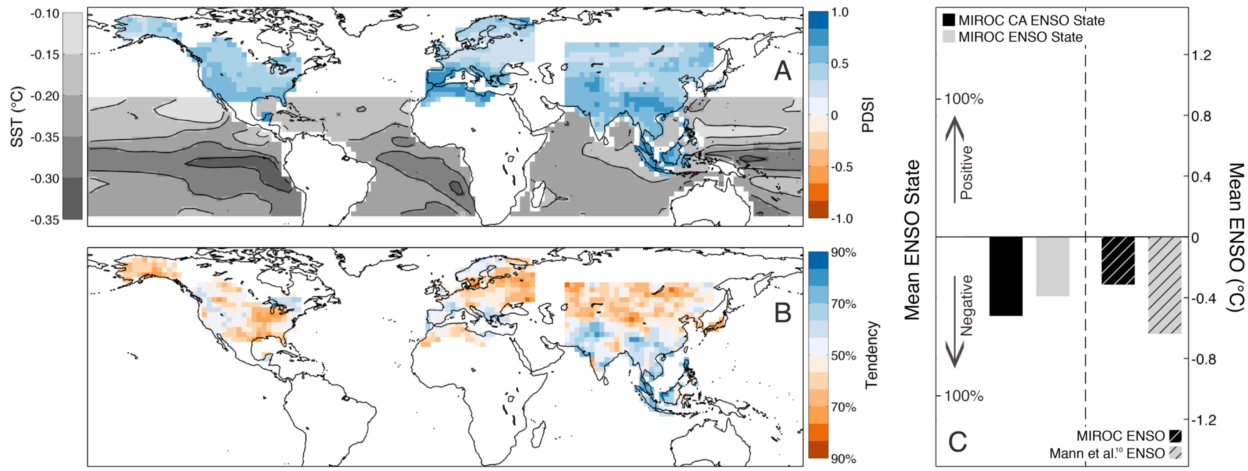

Figure S9. (Panel A) Composite of SST anomalies over the tropical Oceans (30°N to 30°S) between 850-1149 C.E. in the MIROC last millennium simulation relative to 1871-2005 C.E. in the MIROC historical simulation (both from the CMIP5—*Taylor et al.* [*2012*]). Over the NADA, MADA and OWDA domains is the composite PDSI between 850-1149 C.E. in the MIROC last millennium simulation standardized against the 1931-1990 C.E. period in the MIROC historical simulation (the same standardization interval as the NADA). (Panel B) Impact map for a negative ENSO state defined over the 1871-2005 C.E. period in the MIROC historical simulation. (Panel C) A climate analogues framework was computed for the MIROC last millennium simulation (850-1149 C.E.) using impact maps defined over the 1871-2005 C.E. period in the MIROC historical simulation, all other choices follow the pseudoproxy experiments in Text S2 Section A. The mean of the ENSO output of this climate analogues framework between 850-1149 C.E. as compared to the model ground truth. The hatched bars on the right hand side of Panel C show the mean of Niño3.4 index between 850-1149 C.E. in the MIROC last millennium simulation relative to 1871-2005 C.E. in the MIROC historical simulation as compared to the mean of the Niño3 index during the MCA (1000-1299 C.E.) implied by *Mann et al.* [*2009*].

Modeling Center	Institute ID	Model Name
National Center for Atmospheric Research	NCAR	CCSM4*
NASA Goddard Institute for Space Studies	NASA GISS	GISS-E2-R*
Institute Pierre-Simon Laplace	IPSL	IPSL-CM5A-LR*
Max-Planck-Intitut für Meteorologie (Max Planck Institute for Meteorology)	MPI-M	MPI-ESM-P*
Japan Agency for Marine-Earth Science and Technology, Atmosphere and Ocean Research Institute (The University of Tokyo), and National Institute for Environmental Studies	MIROC	MIROC-ESM^

*Pre-industrial control simulation ^Last millenium simulation

Table S1. Model information for the analyzed CMIP5 simulations.

Date (search radius)	ENSO	PDO	AMO	NAO
1000 C.E. (150 km)	0.64	0.79	0.75	0.68
1000 C.E. (300 km)	0.60	0.84	0.84	0.67
1000 C.E. (450 km)	0.76	0.73	0.79	0.74
1250 C.E. (150 km)	0.59	0.82	0.76	0.70
1250 C.E. (300 km)	0.71	0.84	0.78	0.84
1250 C.E. (450 km)	0.71	0.79	0.80	0.77

Table S2. The fraction of years in which the dynamical timeseries from the climate analogues framework have the same sign as observations of these modes of variability between 1871-2005 C.E. The climate analogues frameworks are calculated using only grid points within a fixed distance (search radius) of available tree-ring sites in the years 1000 C.E. (beginning of the analysis period) or 1250 C.E. (starting year of the MADA).

Averaging Period	GRA/Vieira	GRA/Shapiro	CEA/Vieira	CEA/Shapiro
MCA megadroughts	1365.6	1365.1	1365.7	1365.2
1000-2000 C.E.	1365.7	1365.3	1365.7	1365.3

Table S3. Average solar and volcanic forcing (in W/m^2—timeseries are plotted in the bottom panel of Figure 1A) for the MCA megadroughts and the 1000-2000 C.E. period.